

## Constitutive response of welded HSLA 100 steel

Q. Xue<sup>a</sup>, D. Benson<sup>a</sup>, M.A. Meyers<sup>a</sup>, V.F. Nesterenko<sup>a</sup>, E.A. Olevsky<sup>b,\*</sup>

<sup>a</sup> Department of Mechanical and Aerospace Engineering, University of California, San Diego, CA 92093-0411, USA

<sup>b</sup> Department of Mechanical Engineering, College of Engineering, San Diego State University, 5500 Campanile Drive, San Diego, CA 92182-1323, USA

Received 5 August 2002; received in revised form 12 December 2002

### Abstract

The dynamic mechanical behavior of a welded joint of high-strength, low alloy (HSLA) 100 steel was investigated by both quasi-static ( $103 \text{ s}^{-1}$ ) and high strain rate ( $103 \text{ s}^{-1}$ ) tension loadings at ambient and low temperatures. The constitutive responses for the microstructurally different weld and base steels, along with the interface, which included the heat-affected zone (HAZ), were analyzed and compared. This response is successfully modeled by the mechanical threshold stress (MTS) constitutive equation for different regions of the welded joint, which shows qualitatively different behavior. The necking and failure occurred uniformly within the weld metal but not in the HAZ. The main mechanism for the failure of the welded joints is void growth. Microstructural characterization revealed that the nucleation of voids occurred mainly at the interface between the base and the weld metal, and initiated at inclusions. Measurements of damage distributions across HAZ were made to evaluate the contribution of porosity variation to the constitutive response. In both the quasi-static and dynamic tests, the deformation localization in the form of necking first appeared in the weld metal. Fractographic observation demonstrates that void evolution is a dominant factor in the macroscopic mechanical response. The Gurson–Tvergaard model was included in the modeling effort to incorporate the effect of void opening on the mechanical response as well as tensile instability. The MTS constitutive model was successfully implemented to the tensile regime of loading.

© 2003 Elsevier Science B.V. All rights reserved.

*Keywords:* Welding; Constitutive behavior; Failure mechanism

### 1. Introduction and objectives

High-strength, low alloy (HSLA) steels have been widely used in the construction of buildings, pipelines and ships [1–5]. The principal advantages of these materials are not only their good combination of strength and toughness, but also their good weldability. Therefore, the HSLA steel is suitable for applications in large-scale welded steel structures. Such structures, e.g. submarine hulls (or other naval vessels), may be subjected to dynamic loading from impact or explosion. Failure initiation is frequently found in the heat-affected and welded zones [6], and is principally caused by tensile stresses.

HSLA 100 is a special structural steel in the HSLA family, with composition providing a yield stress of up

to 100 ksi (690 MPa). Its good weldability and lack of preheat requirement provide a great convenience for the construction of large-scale structures, and significantly reduce the processing costs. A considerable number of investigations on the properties of HSLA steels and their welding have been carried out in the past 30 years [7,8]. The main concern in these studies is the quasi-static mechanical response, fracture behavior and the metallurgical properties and characteristics of welded joints [9,10]. However, very limited results can be found on the mechanical response of welded joints under dynamic loading. Among these results, the main method to evaluate dynamic properties of a weldment is the pre-cracked Charpy V-notch impact test. Logsdon [11] and Hahn and Kanninen [12] investigated the weldment integrity of structural steels using this method. They evaluated the dynamic fracture behavior through the measurement and analysis of dynamic fracture toughness. Rajanna et al. [13] carried out a series of Charpy tests to examine the fracture toughness for the base,

\* Corresponding author. Tel.: +1-619-594-6329; fax: +1-619-594-3599.

E-mail address: olevsky@kahuna.sdsu.edu (E.A. Olevsky).

weld areas as well as the HAZ, and correlated the fracture behavior to the grain size. The dynamic crack propagation in the weld area was also addressed [14]. Although the Charpy test can provide important information about dynamic fracture, it is hard to obtain the exact dynamic response and microstructural evolution during the dynamic loading process.

The heat-affected zone (HAZ), which is cooled at different rates and includes different regions of microstructure, is often considered the source of failure in a welded joint. During the welding thermal cycle, base steel close to the fusion area will transform to austenite, martensite, ferrite and/or bainite, depending on the cooling rate [15,16] and steel composition. These different phase microstructures correspond to different mechanical properties [6,17,18]. A weld joint consists of fusion weld area, the HAZ and base area (unwelded). Even though some phases in the HAZ show their brittleness and sensitivity to the microcracks, one cannot assume that the initiation of the failure is always in the HAZ. The source and mechanisms of failure for a weld joint without pre-defects under uniform dynamic loading still need to be investigated and the strain rate sensitivity of fracture mechanism cannot be excluded.

The simpler empirical constitutive equations that realistically predict the material behavior in the modeling of the response in engineering applications under different strain rate (such as the Johnson–Cook [19]), have successfully been replaced by dislocation-based equations, such as the Zerilli–Armstrong [20,21] and the mechanical threshold stress (MTS) [22,23]. For a comparison of the characteristics and performance of these equations, see Ref. [24]. These equations are implemented into large-scale computational codes to model the structural response. This approach does not incorporate effects of defects and damage accumulation inside the materials, and these influences have to be separately dealt with. An analytical treatment for defects was developed by Gurson [25], which involves the formation of voids and their weakening effect. The Gurson model was modified by Tvergaard [26]. Fyfe [27] discussed the application of the Gurson model to dynamic failure. Essentially, the Gurson–Tvergaard model involves the opening of voids inside the metal and the attendant loss of load-bearing ability, leading at a sufficient strain, to total fracture.

The objective of this investigation is to characterize the mechanical response of HSLA 100 steel in the temperature range encountered by naval vessels. Of particular importance is the response to underwater explosions, which generate large pressure pulses. Therefore, only ambient- and low-temperature tests were carried out. Low- and high- strain rate tensile tests were carried out in order to provide the parameters for implementation into the MTS constitutive equation. The differences in response among the base, interface

and weld regions are interpreted in terms of microstructural characteristics and are incorporated into the constitutive equation. The mechanism of failure for the weld joint was analyzed and explained with these microstructural characteristics.

## 2. Experimental

### 2.1. Material

The material for the weldment used in these experiments is an HSLA 100 steel, although some of its alloy components do not remain at the low alloy level. The chemical compositions of the HSLA 100 steel plate and the wire electrodes are provided by Naval Surface Warfare Center and are shown in Table 1. The HSLA 100 steel plates with 1 in. (25 mm) thickness were welded at Carderock Navy Laboratory with single V-shape of weld pool by the manual arc-welding technique. The microstructural overview of the weldment is given in Fig. 1. The microstructure exhibits three distinguishing areas: the fusion weld area, the HAZ and the base metal area. Nineteen weld passes were applied to complete the

Table 1  
Compositions of HSLA 100 base steel and electrode 100S-1

	Material	Composition
HSLA 100	C	0.06
	Mn	0.75–1.05
	P	0.020
	S	0.060
	Si	0.40
	Ni	1.50–2.00
	Cr	0.45–0.75
	Mo	0.30–0.55
	Cu	1.00–1.30
	Al	0.010
	Cb	0.02–0.06
	V	0.03
	Ti	0.02
	Sn	0.030
As	0.025	
Sb	0.025	
N		
Electrode 100S-1	C	0.08
	Mn	1.25–1.80
	P	0.012
	S	0.008
	Si	0.20–0.55
	Ni	1.40–2.10
	Cr	0.30
	Mo	0.25–0.55
	Cu	*
	Al	0.05
	Cb	0.10
V	0.10	
Ti	0.10	

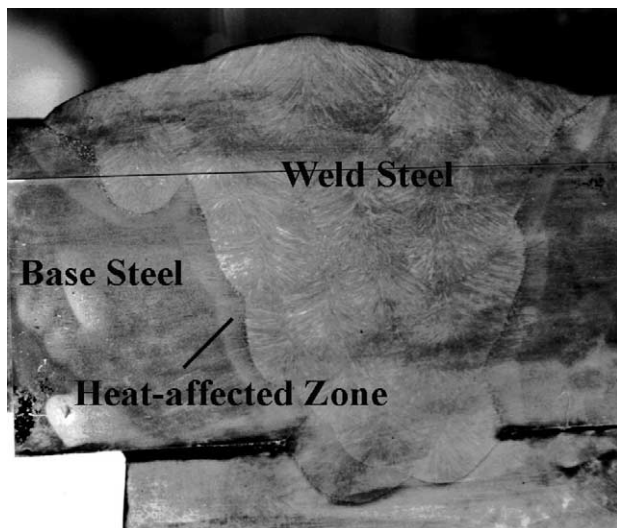


Fig. 1. Microstructural overview of the weld joint.

joining. Their profiles are shown in Fig. 2a. The voltage and the current of the welding are 35 V and 500 A, respectively.

The schematic diagram of the tensile cylinder specimens is shown in Fig. 2b; the gage length and the

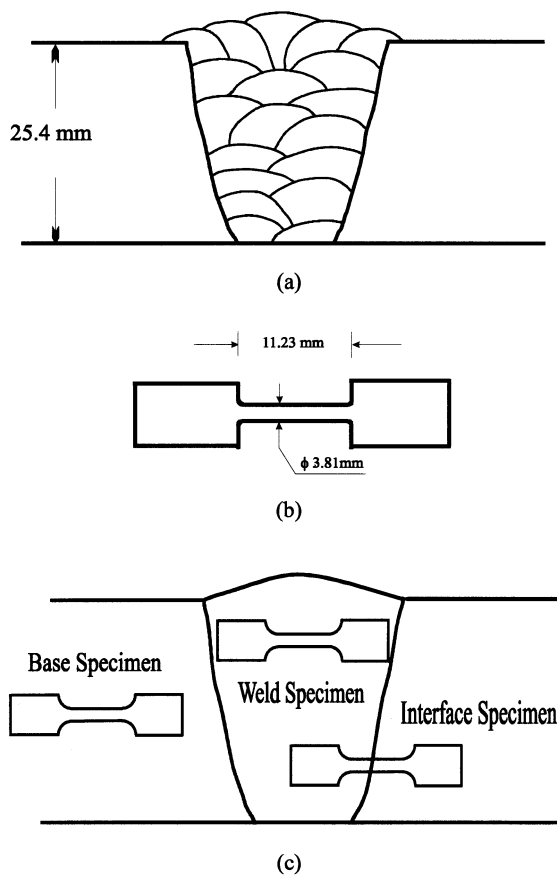


Fig. 2. (a) Welding structure with profiles of welding passes, (b) schematic diagram of the tensile specimens, and (c) selected positions of tensile specimens.

diameter of the specimen were 11.23 and 3.81 mm, respectively. Identical specimens were used for both the quasi-static and dynamic tests. Three types of positions were selected, in order to characterize the properties in three different zones: the base material, the weld material and the interface area that contains the base metal, the weld metal as well as the HAZ. The positions of these specimens are shown in Fig. 2c. The interface specimens were designed to keep the boundary between the weld and the HAZ area perpendicular to the elongation direction of the sample. Since the HAZ is relatively thin (about 1–2 mm), special precautions were made to place it near the center of the specimen.

## 2.2. Mechanical testing

The dynamic tension tests were carried out on a modified Hopkinson tension bar using a momentum trap for reflected compressive waves [28]. The principle and the configuration of the dynamic Hopkinson tension bar are shown in Fig. 3. The modified Hopkinson tension bar can remove most of the wave reverberation after the first loading cycle. This design eliminates the possibility of re-deformation by the secondary wave, using a pre-setting of the gap between the incident bar and the unloading bar. It is very suitable for the recovery tests and the post-examination of the microstructure of the sample [29]. The split Hopkinson tension bar can provide high strain rates up to  $10^3$ – $10^4$   $s^{-1}$ . In this study, the applied strain rate was approximately  $1.6 \times 10^3$   $s^{-1}$ . The quasi-static tests were conducted on an Instron universal-testing machine at a strain rate of  $0.001$   $s^{-1}$ .

The measurements of both macro- and micro-hardness were carried out on the polished sections at room temperature. The macro-hardness measurements were performed in Rockwell C scale (tip load of 150 kg). Across the welding joint area, a set of network points, which are located on the corner knots of a square with an area  $5 \times 5$   $mm^2$ , were selected to determine the distribution of the micro-hardness. The Vickers micro-hardness was measured across HAZ with a load of 500 g and duration of 30 s.

Since the naval ships may sustain low temperatures close to the polar regions, the effects of low temperature on the weldment were studied. Three temperature levels were selected: 298, 190 and 77 K. A special chamber with liquid nitrogen provided the 77 K temperature. The

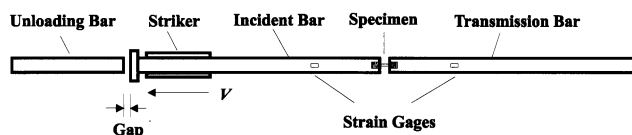


Fig. 3. Principle and the configuration of the dynamic Hopkinson tension bar.

temperature of 190 K was obtained by adding liquid nitrogen into pure methanol to freeze it. A thermocouple was used to monitor the temperature. The goal of the experiments was beyond simply trying to reproduce the experimental conditions that ships experience. Rather, it was to develop a robust constitutive description of the mechanical response of HSLA 100 over a broad range of temperature and strain rates.

### 2.3. Metallography

The microstructure for the base metal, the welded material and the HAZ were examined before and after the tests. The normal metallurgical analysis process was applied through mounting, grinding and polishing. The specimens, etched with 2% nital solution, were examined by both optical and scanning electron microscopies. Damage evolution, especially for the void nucleation, growth and coalesce, was the main concern. In order to reveal the details of the voids and their distribution, the polished samples, without etching, were examined. The void distribution was analyzed by using the image analysis technique.

## 3. Results

### 3.1. Microstructure

The microstructures of the base HSLA 100 plate, the HAZ area and the weld metal are shown in Fig. 4a–c, respectively. The average width of the HAZ is about 2–2.5 mm. The base plate possesses an average grain size of 15  $\mu\text{m}$ , which exhibits a heavily tempered martensite plus acicular ferrite structure. The weld metal in the welding beads has a typical microstructure of proeutectoid ferrite, polygonal Widmanstätten and acicular ferrite, as well as bainite and martensite (shown in Fig. 4c). The proeutectoid ferrite has equiaxed form or thin veins delineating prior austenite grain boundaries. The sideplate Widmanstätten ferrite shows the parallel ferrite laths emanating from prior austenite grain boundaries. The acicular ferrite, which was considered a toughening phase, lies between the bodies of prior austenite grains. HSLA steels are, in addition, characterized by very fine carbonitride precipitates (only visible by TEM), which play a crucial role in strengthening. The low carbon content produces a ductile martensite. In the weld and HAZ regions, the formation of these carbides is seriously hampered.

### 3.2. Hardness distribution and microstructural characterization

Fig. 5 shows the contours of the Rockwell hardness along the sectional direction of the welded plate. It is

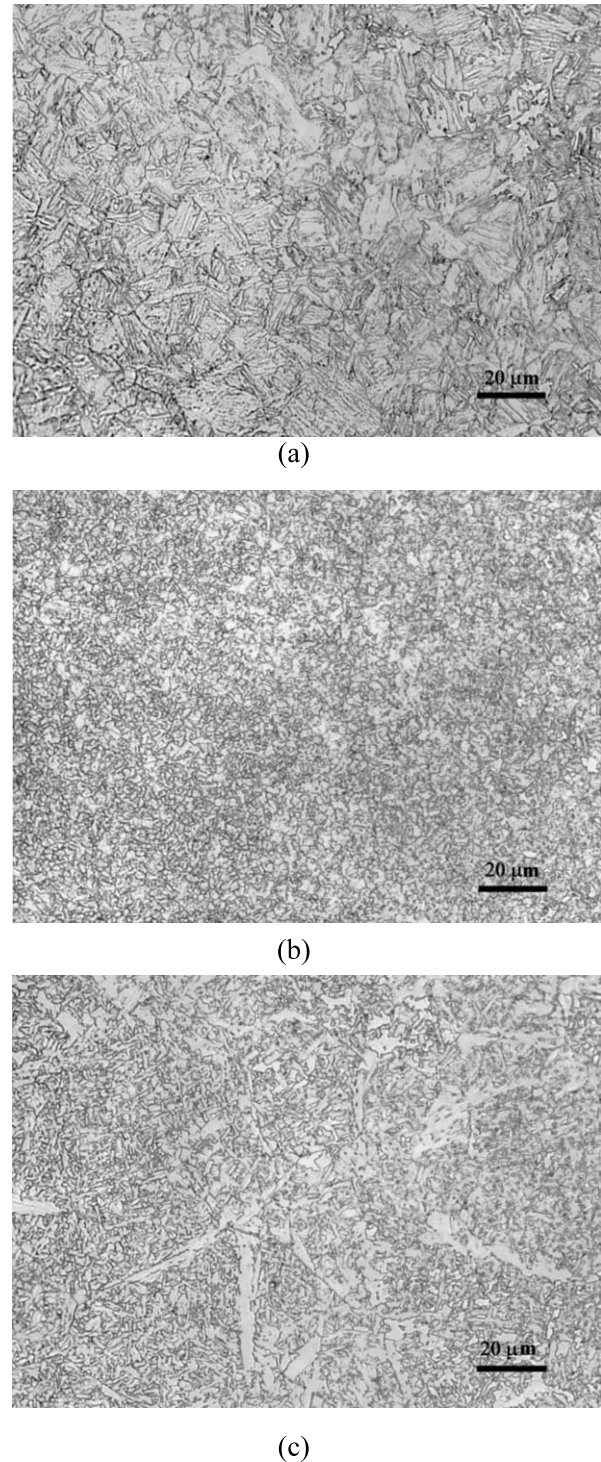


Fig. 4. Microstructures of the welded HSLA 100 joint: (a) the base steel, (b) the weld steel and (c) the HAZ area.

easy to see that the hardness outside the welded area (base plate) is higher than that in the inside area (weld metal). Inside the weld region, the hardness is approximately HRC 19, while the base metal has hardness HRC 25. The points close to the boundary, between the weld steel and the HAZ, show higher hardness than the weld

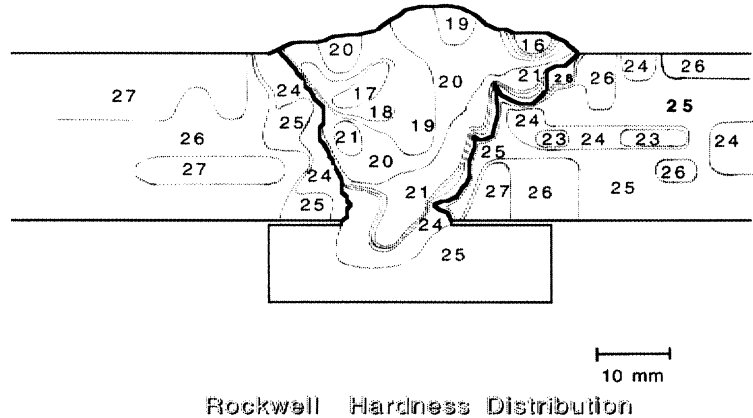


Fig. 5. Rockwell hardness contour map of the measurement in C scale.

center area. Although this map indicates the approximate distribution, it should be pointed out that the variation inside the weld area is not accurately described. A comparison with the microstructural pattern of the sectional welded area reveals that the weld area consists of 19 welding passes (see Fig. 2a). Some tested points are located at the center of the bead and some are located at the boundary between two beads. This measurement may lead to the oversight of the hardness distribution details. Therefore, the hardness measured in the welded area only provides an average distribution and shows the general trends. In addition, the change of the hardness in the HAZ area, approximately 2–2.5 mm in thickness, cannot be described by contour lines, either. So the map only shows that hardness in the welded area is less than that in base plate material. The hardness value close to the right boundary between the weld steel and base steel in Fig. 5 reaches HRC 28, which is much higher than those in both sides. This point is located within the HAZ.

In order to obtain a more detailed view of the material resistance to plastic flow, microindentation hardness measurements were made across the interface. Fig. 6 shows the distribution of Vickers micro-hardness in the HAZ. In the base metal, the hardness remains at HVN  $260 \pm 10$ . The hardness rises as the HAZ is approached from the direction toward the center of the weld area. It reaches the peak value of about 320 HVN at the boundary between the HAZ and the weld metal but in the side of the HAZ. Once the boundary is crossed, the hardness drops down dramatically to HVN 227 and then increases slowly toward the center of the weld bead.

### 3.3. Mechanical response of the welded material

The three quasi-static stress–strain curves in Fig. 7 represent the mechanical responses of the materials from the base metal, the weld metal and their boundary with the HAZ in the center of the specimen. The base metal shows the highest yield stress, while the weld metal gives

the lowest one. This is consistent with the hardness measurements. One can also obtain approximate hardness values from the yield stress, and vice versa, by the conversion  $H/3 = \sigma_y$ . From the micro-hardness, one obtains yield stresses of 860 and 750 MPa for the base and weld areas, respectively. These are fairly close to the flow stresses at a plastic strain of 0.08 in Fig. 7. It is important to emphasize that the tensile test does not capture the small fluctuations in yield stress; the specimen flows in its softest region. It is possible to map the local fluctuations more exactly with hardness measurements. The necking stress is considered to be close to the ultimate peak stress (UPS) point, which gives the transition point from uniform deformation to unstable deformation. The corresponding plastic strain at necking initiation (uniform elongation) is about 0.085 for the weld metal and 0.076 for the base metal. However, the specimen taken from the boundary area shows a

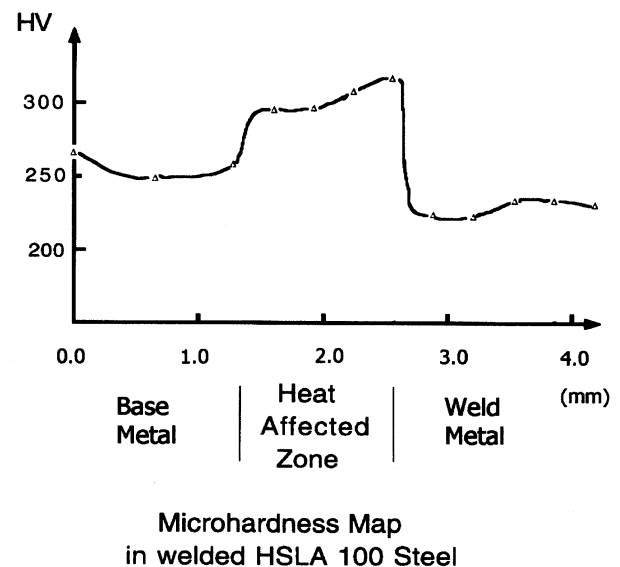


Fig. 6. Detailed distribution of Vickers micro-hardness along the HAZ.

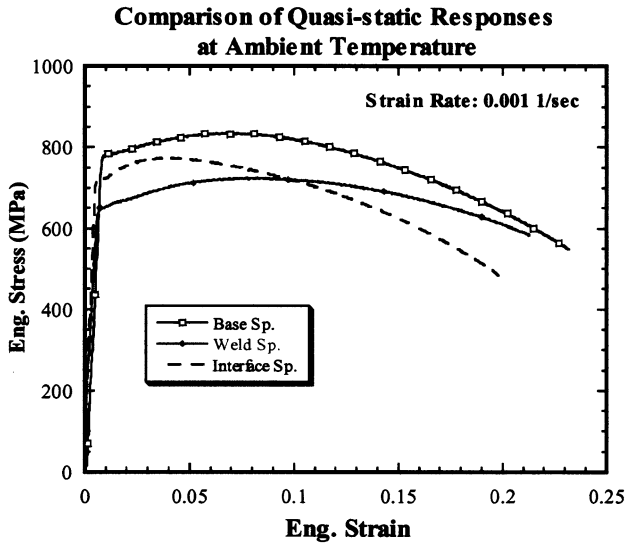


Fig. 7. Quasi-static mechanical responses of base steel, weld steel and boundary with the HAZ in the center of the specimen.

considerably lower uniform elongation (only about 0.04). The reason is the following: the specimen contains base metal, HAZ and weld metal in its gage length and cannot undergo a uniform deformation in tension. The deformation accumulates and localizes faster into the weak section, which results in premature necking. For a specimen containing base metal, weld metal and the HAZ (interface specimen), the weld metal section will yield first, since the base metal has a higher yield stress. Fig. 7 shows that the HAZ should have higher yielding stress than the weld metal, otherwise the stress–strain curve of the interface specimen would have lower yielding point instead of that between the yield points of base and weld metals. The experimental results also show that the necking area is always located in the weld metal region for the interface specimen.

Fig. 8 presents the strain-rate effects for these materials at two strain rates:  $10^{-3}$  and  $10^3$  s $^{-1}$ . The HSLA 100 steel possesses a strong strain-rate sensitivity and the UPS point increases between 15.6 (Fig. 8a; base metal) and 20% (Fig. 8b; weld region). The yield point for the dynamic response is difficult to determine due to the mixing of high strain-rate effect at the front of a loading pulse, instrument response and wave reverberation. In order to determine and compare the flow behaviors, an effective yield point was applied by averaging peak and valley stresses. The effective yielding stress can be used as a replacement for the approximate yielding point to compare the dynamic and quasi-static responses.

The temperature effect is another important factor in the dynamic tension tests. Three testing temperatures, the ambient temperature (298 K), 190 K and 77 K, were chosen for investigating the low-temperature behavior of the weld element. Fig. 9a and b show the mechanical

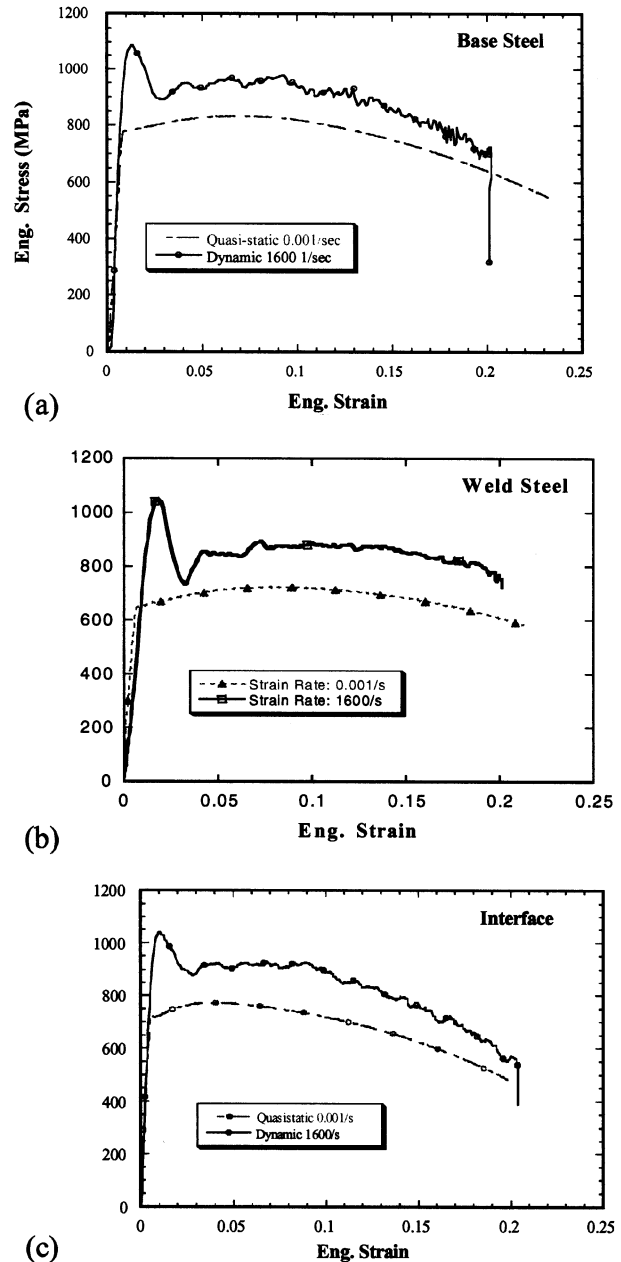


Fig. 8. Effects of the strain rate in the range  $10^{-3}$ – $10^3$  s $^{-1}$ : (a) base steel, (b) weld steel and (c) interface specimen.

behavior of the interface specimen at these temperatures under the loading strain rate of  $10^{-3}$  and  $1600$  s $^{-1}$ . The lower the temperature, the more brittle the material appears. For the liquid nitrogen temperature, the strength and the yielding stress increase about 35 and 53.1%, compared with the quasi-static data. The total elongation under the same loading duration decreases to about 60% of that at ambient temperature. For the 190 K, which is close to the real low-temperature environment in polar areas for naval ship, the strength and yield stress increase about 12 and 23.8%, while the elongation under the same condition decreases by 5%.

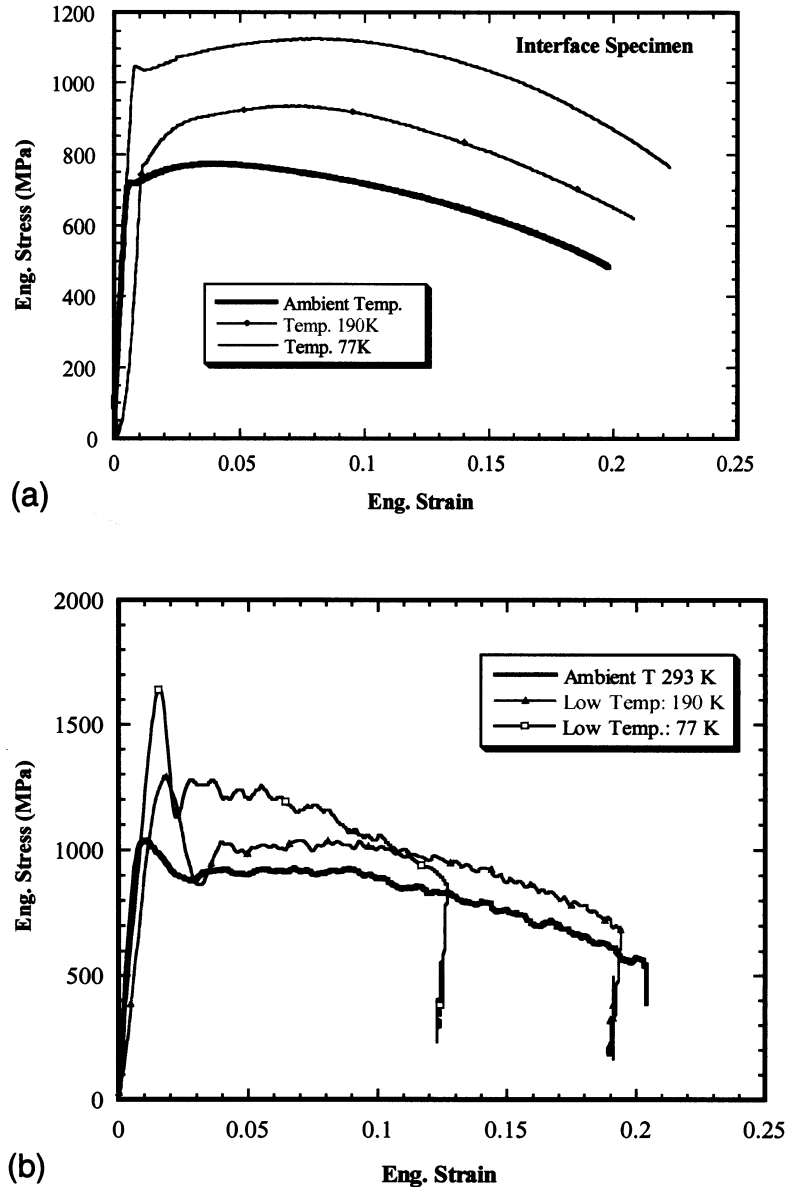


Fig. 9. Temperature effect on the tensile stress–strain behavior (interface): (a) quasi-static mechanical response and (b) dynamic mechanical response.

### 3.4. Microstructure and failure characteristics

All interface specimens under different strain rates and temperatures show that the necking happened inside the welding area. Fig. 10 exhibits a typical sectional view of an interface specimen. The HAZ is marked, and the base metal region and the weld metal region show different metallurgical characters. The deformation quickly localizes into the necking area once the critical stress reached. Within the necking area, the grains were elongated and micro-voids appeared in the inclusion-matrix boundary.

The analysis of fracture surface provides rich information for the failure process. The SEM fractograph of the weld metal after the dynamic deformation is shown

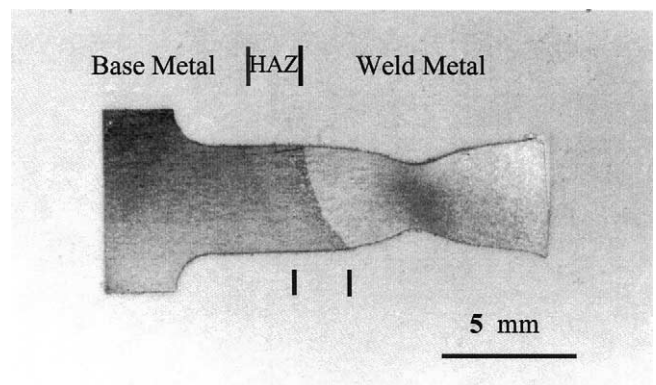


Fig. 10. Failure configuration of the interface specimen. The necking always happens in the weld metal region.

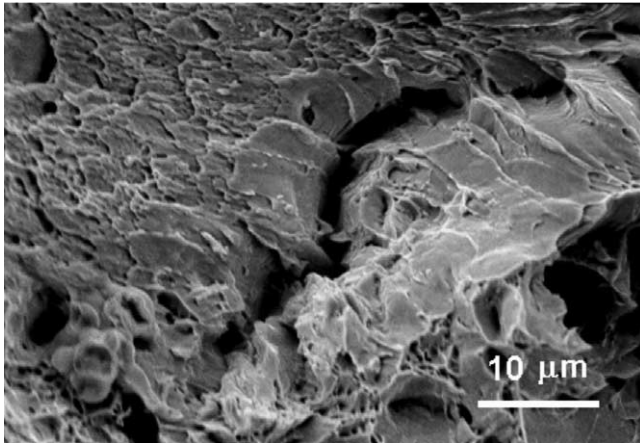


Fig. 11. Fracture surface of the interface specimen at 77 K under dynamic loading.

in Fig. 11. The dimple structure reveals that the fracture character is typically ductile for both loading conditions. The average diameter of dimples in the dynamic tests is about 3.5  $\mu\text{m}$ .

Fig. 11 shows the fracture surface of the interface specimen at 77 K under dynamic loading. The fracture morphology is different from that in Fig. 10. At 77 K, the specimen exhibits cleavage feature accompanied with some dimple structure. The edges of these dimples are very shallow and the density of the dimples is also quite low. A possible mechanism is thermal softening at low temperature. The heavy localization of the deformation in the last stages of the dynamic tension provides a large amount of plastic work that is transferred into heat. The dynamic loading process limits the loading duration in a very short range. Such a short loading duration cannot be enough for the local heat to transport to the adjacent areas. The localized deformation becomes a kind of adiabatic deformation. The local heat production makes the local material soften and behave as ambient features, although its neighbors remain in the low temperature.

The damage form in the weld metal is principally the voids, which has been observed in the fractographic analysis. The high density of the network dimple structure testified that the nucleation and growth of the voids is the main failure mechanism of the weld element. The distribution and evolution of the voids govern the failure process. A series of patterns of void distribution were examined along the necked interface specimen. Fig. 12 shows the initial microscopic impurities in the weld steel. The general shape of the initial impurities is round and relatively uniform, and the average size of the voids is about 2  $\mu\text{m}$ . Since the black pits on the image may be either voids or inclusions, the distribution of such impurities can be measured by porosity or inclusion fraction. In order to get a uniform expression, we select the porosity to describe the distribution of these impurities. Keep in mind in the

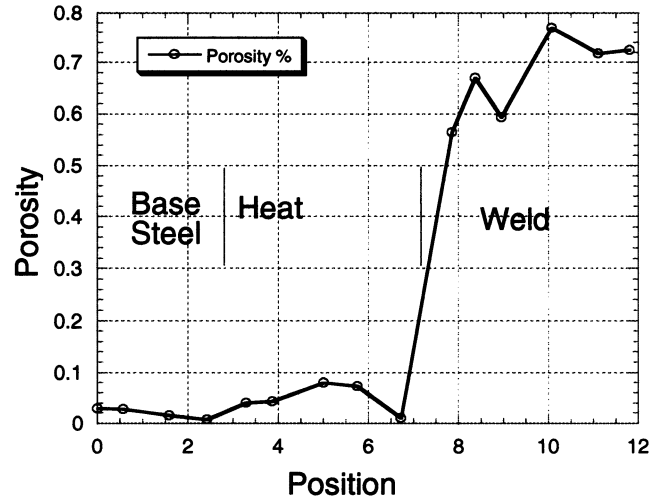
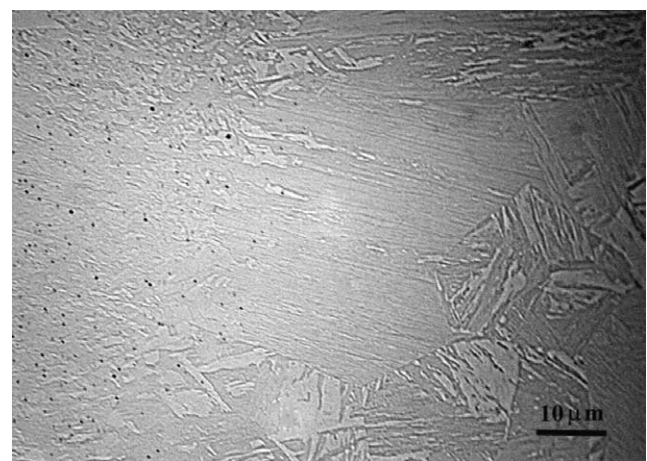


Fig. 12. Distribution of initial microscopic impurities in the specimen.

present paper that “porosity” used here represents the sum of the density of voids and inclusions. The initial distribution of voids along the interface specimen is exhibited in Fig. 12, in which the porosity was described as the function of the position. It is easy to find that the porosity or the inclusion fraction in the base steel and the HAZ are relatively low. A remarkable jump appears on the boundary between the weld metal and the HAZ. The porosity rises to a constant value (0.7%). Fig. 13 shows a detailed discrimination of the impurities on the boundary between the weld steel and the HAZ. The arrow represents the position of the boundary. The black impurities under the background of very shallow microstructure (from fine polishing but without etching surface) give the pattern of the void distribution. It can be concluded that the base steel has very few initial



WELD  
 ↑  
 BOUNDARY  
 HEAT-AFFECTED ZONE

Fig. 13. Impurities (porosity) on the boundary between the weld steel and the HAZ.

defects while the weld steel exhibits a uniform inclusion distribution, which effects the mechanical response.

The porosity was carefully examined after the tensile tests. The porosity distribution along the tested specimen is directly dependent on the strain level of the examined section. The inhomogeneous deformation corresponds to the variation of void density and dimension. After measuring the porosity along the tested section, the maximum porosity is only less than 1.6%, which means that the volume change of the tested specimen is vary small and can be ignored. Based on this assumption, an estimation of the effective strain is given using the following method. Consider the constant volume of the tested section  $dV = l dA + A dl = 0$  and we have  $\varepsilon = \varepsilon_t = \Delta l/l = dA/A = dr/r$ , where  $r$  is the radius of the specimen. The distribution of the porosity and the effective strain in the dynamic tension specimen is shown in Fig. 14. The necking center corresponds to the peak of the porosity. The maximum porosity reaches 1.5% and the maximum void diameter is about 5  $\mu\text{m}$ . The similar characteristics can be found that the porosity in the weld metal is much higher than that in the HAZ and the base metal. The distribution of void microstructure on different section along the specimen is examined at positions 1, 2, 3, 4 and 5 in Fig. 14. Fig. 15a–e give the corresponding microstructure of the void distribution. The center of the necking area (Fig. 15b) shows that the voids have grown and elongated to the ellipse shape with the long axis parallel to the tension direction. This is not similar to the ordinate void growth that shows the long axis perpendicular to the tension direction. This phenomenon seems to grant a clue that the matrix steel is perfectly ductile and the bonding between the steel and the inclusions is relatively weak. Once the voids nucleate around the inclusion, the void is elongated only along the tension direction but with less growth on the normal direction. The porosity of the necking center reaches to 1.58%, which is higher than

both sides shown in Fig. 15a and c. The strain distribution of the interface specimen also corresponds to the distribution of the porosity in the interface specimen. The boundary between the weld steel and the HAZ identically reveals the dramatic variation of impurity distribution on it. It is clear that there is almost no void visible on the other side of the boundary from Fig. 15d and e. The void distribution along the tested specimen indicates that the void nucleation and growth result in deformation localization initially in the weld metal. Both the quasi-static and dynamic tension tests of the interface specimen show that fracture happened in the welded area and that the necking induced from the void growth is the dominant mechanism of failure.

The microstructure observation and fractographic analysis provide enough evidence that the void evolution is the main controlling factor for the failure of the welded HSLA 100 steel. The deformation localization with the form of necking correlates with the development of the voids. Fig. 16 shows the variation of the porosity with the effective strain for a dynamic test at room temperature. The damage in the form of voids increases monotonically with strain if the loading rate and the temperature are fixed. This result offers a simple relation for the prediction of the constitutive behavior.

#### 4. Analytical prediction and comparison with experimental data

The constitutive behavior of the welded material should be described accounting for the presence and evolution of voids. The stress analysis of welded structures has been performed by various authors [30–32]; however, these investigations assumed a constitutive behavior of a fully dense material of both welded and HAZs.

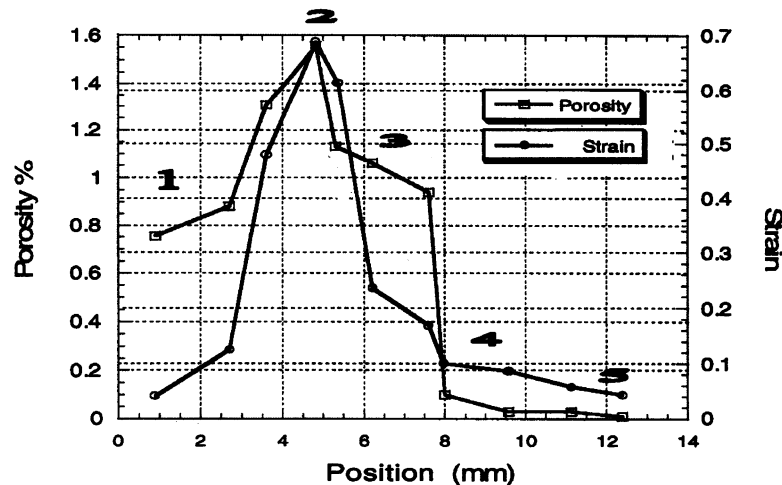


Fig. 14. Distribution of porosity and effective strain in dynamic tension specimen.

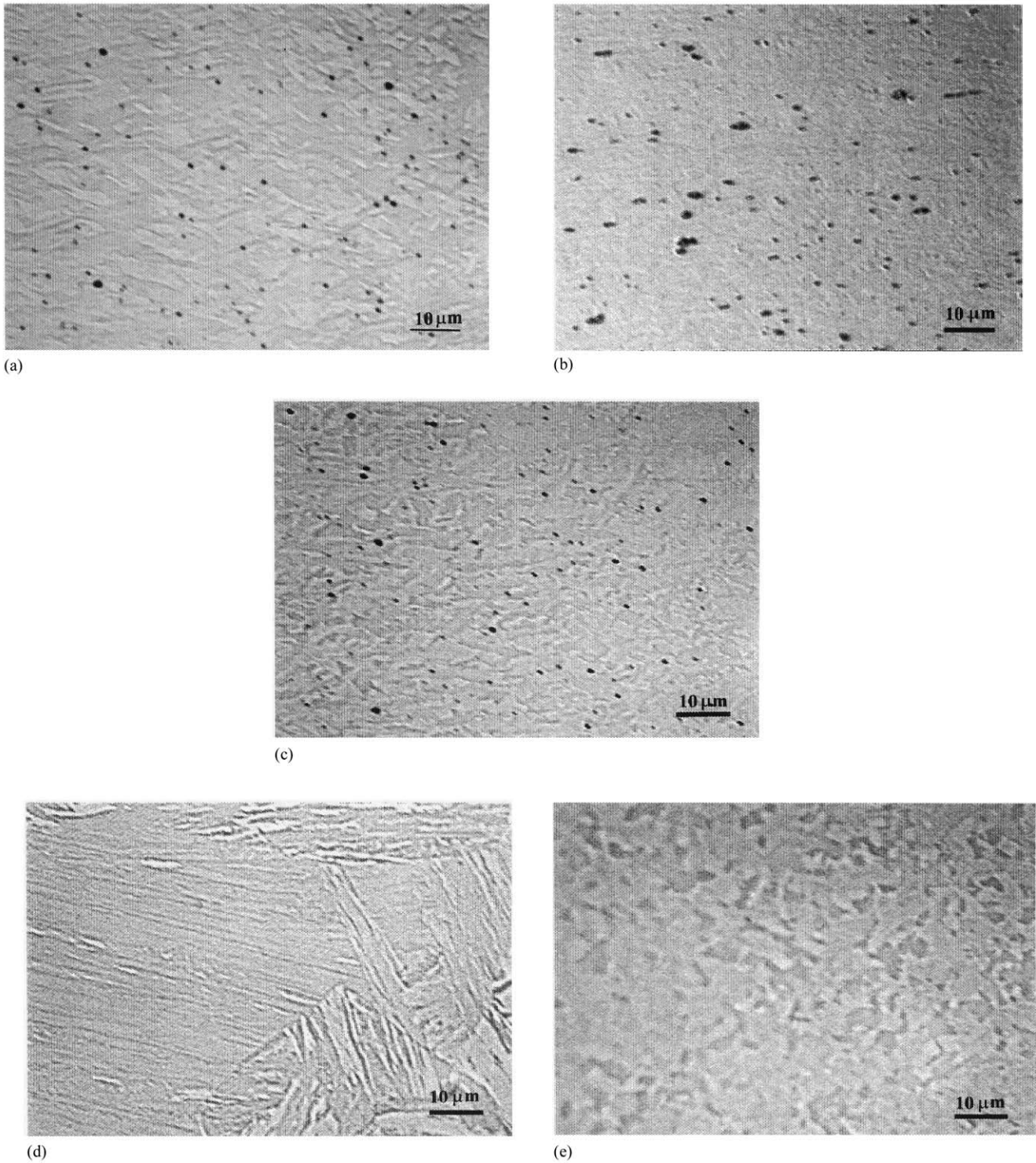


Fig. 15. The corresponding microstructure of the void distribution: (a–e) positions 1–5 on the specimen in Fig. 14.

#### 4.1. Mechanical threshold stress model: constitutive analysis of the solid material

The constitutive response of high-strength steels has been successfully described by the Zerilli–Armstrong and MTS models. Armstrong et al. [33] used the Z–A model

to model the response of HY-80, HY-100 and HY-130 steels; good correspondence was obtained with experimental results, yielding a rationalization of the ductile–brittle transition. For the description of the stress–strain relationships of the steel, the MTS model [22,23] is employed. The corresponding expressions are repre-

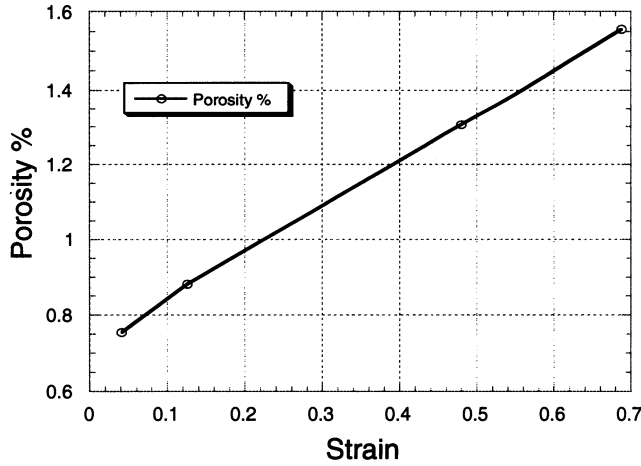


Fig. 16. Variation of porosity as the function of effective strain.

sented below:

$$\frac{\sigma}{\mu} = \frac{\sigma_a + (\sigma - \sigma_a)}{\mu} = \frac{\sigma_a}{\mu} + S_i(\varepsilon, T) \frac{\sigma_i}{\mu_0} + S_\varepsilon(\varepsilon, T) \frac{\sigma_c}{\mu_0}, \quad (1)$$

where

$$S_i(\varepsilon, T) = \left\{ 1 - \left[ \frac{kT}{g_{0i}\mu b^3} \ln \left( \frac{\varepsilon_{0i}}{\varepsilon} \right) \right]^{1/q_i} \right\}^{1/p_i}, \quad (2)$$

$$S_\varepsilon(\varepsilon, T) = \left\{ 1 - \left[ \frac{kT}{g_{0\varepsilon}\mu b^3} \ln \left( \frac{\varepsilon_{0\varepsilon}}{\varepsilon} \right) \right]^{1/q_\varepsilon} \right\}^{1/p_\varepsilon}. \quad (3)$$

The work hardening is given by

$$\frac{d\widehat{\sigma}_\varepsilon}{d\varepsilon} = \theta_0(\varepsilon, T) \left[ 1 - \frac{\tanh \left( \alpha \frac{\widehat{\sigma}_\varepsilon}{\widehat{\sigma}_{\varepsilon s}(\varepsilon, T)} \right)}{\tanh(\alpha)} \right], \quad (4)$$

where  $\sigma$ ,  $\varepsilon$  and  $\dot{\varepsilon}$  are the flow stress, strain and strain rate under uniaxial tension, respectively.  $\mu$ ,  $g_0$ ,  $\varepsilon_0$ ,  $q$ ,  $p$  and  $\alpha$  are the material parameters.  $\sigma$  is the MTS and  $\sigma_a$ ,  $\sigma_i$ , and  $\sigma_\varepsilon$  are its athermal (first) and thermal components (latter two). The subscripts  $i$  and  $\varepsilon$  correspond to the contribution of the thermal component from the intrinsic barriers (dislocations and defects) and from dislocation interactions, respectively.  $\sigma_{\varepsilon s}$  represents the saturation stress.  $k$  is the Boltzmann constant,  $b$  the Burgers vector and  $T$  the absolute temperature (K). The values of  $p_i$  and  $q_i$  were taken as 1/2 and 3/2, respectively, in accordance with Ref. [34]. Table 2 shows the values that were used in the implementation of the MTS Model. They are based on Chen and Gray [35], who applied the model to a fairly similar alloy, HY-100. The parameters were modified to fit for our alloy, HSLA 100. The principal changes are a reduction in the athermal stress,  $\sigma_a$ , from 350 to 200 MPa and 50 MPa for the base and weld steels, respectively;  $\sigma_i$  from 1338 to 1200 MPa for both base and weld steels; the strain hardening coefficient from 3500 to 1200 MPa (for base steel) and 2500 MPa (for weld steel). The above-

Table 2  
Principal parameters for theoretical prediction of MTS model

Parameters	Symbol	Values	
		Base	Weld
Rate-independent threshold stress	$\sigma_a$ (MPa)	200	50
Normalized activation energy 1	$g_{0es}$ (J)	1.600	
Normalized activation energy 2	$g_{0i}$ (J)	0.698	
Sigma1 sub I	$\sigma_i$ (MPa)	1200	1200
Thermal activation equation constant-i	$\varepsilon_{0i}$ ( $s^{-1}$ )	1.00E+09	
Thermal activation equation constant-e	$\varepsilon_{0e}$ ( $s^{-1}$ )	1.00E+07	
Normalized activation energy 3	$g_{0e}$ (J)	1.60E+00	
Initial threshold stress	$\sigma_0$ (MPa)	0.000	
Saturation stress at zero degrees K	$\sigma_{s0}$ (MPa)	750.000	
Saturation stress reference strain rate	$\varepsilon_{s0}$ ( $s^{-1}$ )	1.00E+07	
Free energy equation exponent	$p$	0.667	
Free energy equation exponent	$q$	1.000	
Hardening function constant	$a_1$	3000.000	
Hardening function constant	$a_2$	-2.644	
Hardening function constant	$a_3$	18.581	
Ambient temperature	$T_0$ (K)	298.000	
Boltzmann's constant	$k$	1.36E+00	
Poisson's ratio	$\nu$	3.40E-01	
Youngs modulus	$E$ (MPa)	1.86E+05	
Strain rate	( $s^{-1}$ )	1600	
Strain hardening factor	(MPa)	1200	2500
Density of material	$\rho_0$	7.86E+00	
Specific heat A0	$c_0$	0.09278	
Specific heat A1	$c_1$	7.45E-04	
Specific heat A2	$c_2$	12404	
Alpha	$\alpha$	1	

All parameters from central column are taken from Ref. [35].

mentioned material parameters were used for the regression of the experimental data of the dynamic tests given in Fig. 17. The determination of these parameters is based on our experimental results. Comparing the quasi-static testing data of the base and weld steel in Fig. 17a and b, the base steel shows a higher strength during the tension, while the weld steel exhibits a stronger work hardening effect. The experimentally obtained curves were fitted by the regression curves based upon the MTS model (1). The match between experimental and analytical results is good at low strain; at higher strains (0.1) the two curves diverge significantly, since void opening occurs in the experiments, which is not represented by the analytical model. The results of this approximation are shown in Fig. 17. The modeling results indicate a monotonic increase of the stress with strain. No structure instability effects are involved in the analysis at this level. Both the stress initial value and the stress increase rate are higher for the material outside the weld.

#### 4.2. Gurson–Tvergaard model: constitutive analysis of the porous material

The loading surface in accordance with the Gurson–Tvergaard model [27] can be described by the following relationship:

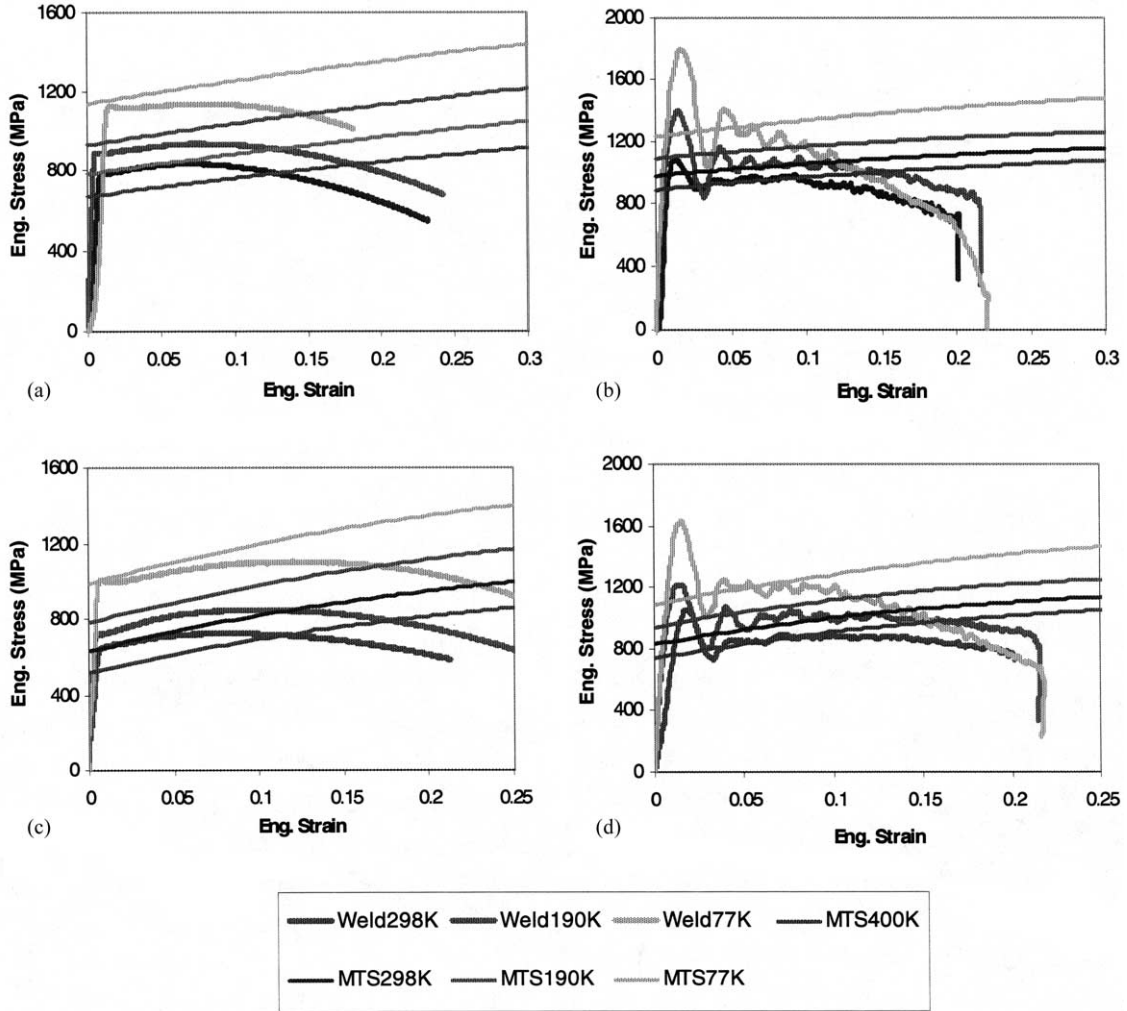


Fig. 17. Comparison between the experimental and the calculated (MTS) stress–strain curves for quasi-static and dynamic results: (a, b) base steel; (c, d) welded region.

$$\frac{\sigma_e^2}{\sigma_m^2} = 2q_1 \cosh\left(\frac{q_2}{2} \frac{\sigma_{kk}}{\sigma_m}\right) - (1 - q_3\theta^2) = 0, \quad (5)$$

where  $\sigma_e$  and  $\sigma_{kk}$  are the deviatoric and hydrostatic stresses, respectively,  $\sigma_m$  is a matrix (porous body) yield stress,  $\theta$  is the porosity, and  $q_1, q_2, q_3$  are the Tvergaard parameters. For  $q_1 = q_2 = q_3 = 1$ , the Gurson–Tvergaard model [27] reduces itself to the Gurson model [28].

For the description of a uniaxial-loading test, the dependencies between the stress tensor invariants and axial stress are used in the form ( $\sigma_z$  is the stress along the loading direction):

$$\sigma_{kk} = \frac{\sigma_z}{3}, \quad \sigma_e = \sqrt{\frac{2}{3}}\sigma_z. \quad (6)$$

Substituting Eq. (6) into Eq. (5), one obtains

$$q_3\theta^2 - \left\{ 2q_1 \cosh\left[\frac{q_2}{6} \frac{\sigma_z}{\sigma_m}\right] \right\} \theta + 1 - \frac{2\sigma_z^2}{3\sigma_m^2} = 0. \quad (7)$$

In the Gurson–Tvergaard model, the value of  $q_1$  is fixed:  $q_1 = 1.5$ . The other two parameters  $q_2$  and  $q_3$  can be determined using the experimental data represented in Fig. 17c and d. Eq. (7) describes the relationship between the axial stress and porosity under conditions of uniaxial testing. In order to derive the stress–strain relationship, one needs to incorporate axial strain as another independent variable (instead of porosity) in Eq. (7). The following expressions enable the solution of the above-mentioned problem:

$$\frac{\Delta V}{V} = \frac{\theta - \theta_0}{1 - \theta} = \varepsilon_z + 2\varepsilon_r, \quad (8)$$

where  $\Delta V/V$  is volume shrinkage,  $\theta_0$  the initial porosity,  $\varepsilon_z$  and  $\varepsilon_r$  are the axial and radial strains, respectively,  $\nu$  ( $= -\varepsilon_r/\varepsilon_z$ ) the Poisson ratio.

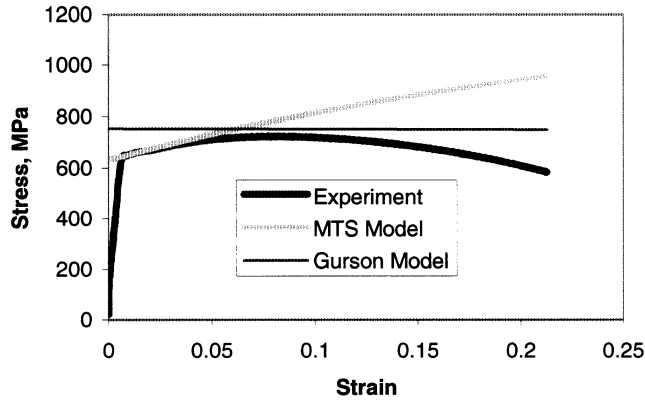


Fig. 18. MTS model, Gurson–Tvergaard model prediction and experimental curves.

It follows from Eq. (8) that

$$\varepsilon_z = \frac{\theta - \theta_0}{(1 - \theta)(1 - 2v)}. \quad (9)$$

Among the variety of the expressions describing the dependence of Poisson's ratio on porosity, the following relationship was chosen:

$$v = \frac{2 - 3\theta}{4 - 3\theta}. \quad (10)$$

The parameters  $q_2$  and  $q_3$  can be fitted by using the experimental data from Fig. 17c. For example, for the temperature of 298 K,  $q_2$  is found to be  $\sim 20$  and  $q_3$  is  $\sim 0.45$ . The initial porosity in Eq. (11) is accepted to be 0.016 (see Section 3.3). The fitting algorithm is described by the following scheme:

$$\left. \begin{array}{l} \theta \text{ (Eqs. (10) and (11))} \\ \varepsilon_z \Rightarrow \sigma_m \text{ (from MTS)} \\ \sigma_z \text{ (from experiments)} \end{array} \right\} \Rightarrow q_2, q_3, \quad (11)$$

where the left-hand side of Eq. (7) should be as close to zero as possible. The above-mentioned values of  $q_2$  and  $q_3$  were substituted into Eq. (7) and compared for the curves corresponding to the MTS model and experimental data shown in Fig. 18. One can see that, due to the small value of porosity, the softening effect introduced by the Gurson–Tvergaard mechanism is minimal. Hence, the decrease of the yield stress observed in the experiments should be attributed to the formation of a diffuse neck through tensile instability.

## 5. Conclusions

(1) The dynamic mechanical behavior of the welding joint in HSLA 100 steel was investigated over a broad range of temperatures and strain rates.

(2) Both quasi-static and dynamic tension tests were carried out to evaluate the mechanical responses and to obtain the parameters required in the MTS constitutive equation. Additionally, the damage distribution was examined in the weld metal, base metal and HAZ. The Gurson–Tvergaard model was included to incorporate the effect of void opening on the mechanical response.

(3) As is the case with many alloys containing second-phase particles, they act as initiation sites for voids. It was confirmed that the higher concentration of initial impurities in the welded region provides initiation sites for voids and weakens the weld joint. The voids nucleate first around the inclusions and grow during the tension process. In both the quasi-static and dynamic tests, the deformation localization in the form of necking first appeared in the weld metal. Fractographic observation demonstrates that the void evolution is a dominant factor in the macroscopic mechanical response. Therefore, failure occurs preferentially in the weld zone for both quasi-static and dynamic tests.

(4) At 77 K, the material exhibits a low ductility, and failure is of a mixed ductile–brittle mode.

(5) The dynamic response was successfully modeled by using the MTS constitutive equation. The Gurson–Tvergaard void failure model was included in the modeling effort to incorporate the effect of void opening on the mechanical response. It was found that void growth plays a minimal role and softening is due to diffuse necking.

(6) The results of the combined MTS–Gurson–Tvergaard model agree well with the experimental results and provide the basic parameters for input into large-scale computational codes.

## Acknowledgements

This research program was funded by the Office of Naval Research Contract ONR N00014-96-1-063 with Dr. L. Couchman as the program manager. We thank Dr. G. Yoder, ONR, for his continued interest. We also thank Mr. J. Isaacs, Mr. David Lischer and Mr. Weiguo Guo for their kind assistance on experiments in the Center of Excellence for Advanced Materials. Discussions with Dr. E.J. Czyryca and Dr. G.T. Gray III in LANL, and Professor Sia Nemat-Nasser, CEAM, are gratefully acknowledged.

## References

- [1] E.J. Czyryca, R.E. Link, R.J. Wong, D.A. Aylor, T.W. Montemarano, J.P. Gudas, Nav. Eng. J. 102 (1990) 63–82.
- [2] T.W. Montemarano, B.P. Sack, J.P. Gudas, M.G. Vassilaros, H.H. Vanderveldt, J. Ship Prod. 22 (1986) 145–162.
- [3] P.W. Holsburg, J.P. Gudas, I.L. Caplan, Adv. Mater. Process. 138 (1) (1990) 45–49.

- [4] S.W. Thompson, D.J. Colvin, G. Krauss, *Metall. Mater. Trans. A* 27 (1996) 1557–1571.
- [5] M. Manganello, in: *Proceedings of the International Conference on Processing, Microstructure and Properties of Microalloyed and other Modern HSLA Steels*, ISS-AIME, Warrendale, PA, 1992, pp. 331–343.
- [6] G. Spanos, R.W. Fonda, R.A. Vandermeer, A. Matuszeski, *Metall. Mater. Trans. A* 26 (1995) 3277–3293.
- [7] K. Hulka, F. Heisterkamp, *Mater. Sci. Forum* 284–286 (1998) 343–350.
- [8] L. Parilak, J. Dojcak, *Int. J. Pressure Vessels and Piping* 73 (7–8) (1993) T761–T765.
- [9] G.E. Hicho, S. Singhal, L.C. Smith, R.J. Fields, in: *Proceedings of the International conference on Tech. and Appl. of HSLA Steels*, American Society for Metals, Metals Park, OH, 1984, pp. 705–713.
- [10] P.E. Denney, E.A. Metzbowler, in: *Proceedings of the International Conference on Tech. and Appl. of HSLA Steels*, American Society for Metals, Metals Park, OH, 1984, pp. 689–696.
- [11] W.A. Logsdon, *Eng. Fracture Mech.* 16 (1982) 757–767.
- [12] G.T. Hahn, M.F. Kanninen, *Eng. Fracture Mech.* 14 (1981) 725–740.
- [13] K. Rajanna, S.K. Bhambri, D.R.G. Achar, *Eng. Fracture Mech.* 29 (4) (1988) 387–399.
- [14] Y.W. Shi, Z.X. Han, N.N. Zhou, J. Li, *Eng. Fracture Mech.* 41 (1) (1992) 143–151.
- [15] M. Mujahid, A.K. Lis, C.I. Garcia, A.J. DeArdo, in: *Proceedings of the International Conference on Processing, Microstructure and Properties of Microalloyed and other Modern HSLA Steels*, ISS-AIME, Warrendale, PA, 1992, pp. 345–356.
- [16] O. Grong, D.K. Matlock, *Int. Mater. Rev.* 31 (1) (1986) 27–48.
- [17] P.L. Harrison, R.A. Farrar, *Int. Mater. Rev.* 34 (1) (1989) 35–51.
- [18] G. Thewlis, *Mater. Sci. Technol.* 10 (1994) 110–125.
- [19] G.R. Johnson, W.H. Cook, in: *Proceedings of the Seventh International Symposium on Ballistics*, Am. Def. Prep. Org. (ADPA), The Netherlands, 1983.
- [20] F.J. Zerilli, R.W. Armstrong, *J. Appl. Phys.* 61 (1987) 1816–1825.
- [21] F.J. Zerilli, R.W. Armstrong, *J. Appl. Phys.* 68 (1990) 1580–1591.
- [22] P.S. Follansbee, in: L.E. Murr, K.P. Staudhammer, M.A. Meyers (Eds.), *Metallurgical Applications of Shock-wave and High-strain Rate Phenomena*, Dekker, New York, 1986, pp. 451–479.
- [23] P.S. Follansbee, U.F. Kocks, *Acta Met.* 36 (1988) 81–93.
- [24] M.A. Meyers, *Dynamic Behavior of Materials*, Wiley, New York, 1994, pp. 318–323.
- [25] A.L. Gurson, *J. Eng. Mater. Technol.* 99 (1977) 2–15.
- [26] V. Tvergaard, *Ductile fracture by cavity nucleation between large voids*, Report 210, Danish Center for Appl. Math. and Mech., 1981.
- [27] I.M. Fyfe, in: J. Mescal, V. Weiss (Eds.), *Material Behavior under High Stress and Ultrahigh Loading Rates*, 1983, pp. 309–318.
- [28] S. Nemat-Nasser, J.B. Isaacs, J.E. Starrett, *Proc. R. Soc. London A* 435 (1991) 371–391.
- [29] A. Thakur, S. Nemat-Nasser, K.S. Vecchio, *Acta Mater.* 44 (1996) 2797–2807.
- [30] J. Ronda, G.J. Oliver, *Comput. Meth. Appl. Mech. Eng.* 153 (3–4) (1998) 195–221.
- [31] Z. Wang, T. Inoue, *Mater. Sci. Technol.* 1 (10) (1985) 899–903 (Calculation of Internal Stresses in Heat treatment of Metallic Materials, Linköping, Sweden, 23–25 May 1984).
- [32] G. Horhoianu, D.R. Moscalu, I.A. Popescu, *Nucl. Eng. Des.* 168 (1–3) (1997) 319–323.
- [33] R.W. Armstrong, F.J. Zerilli, W.H. Holt, W. Mock Jr., in: S.C. Schmidt, et al. (Eds.), *High-pressure Science and Technology—1993*, AIP Conference Proceedings, Vol. 309, Part 2, AIP Press, New York, 1994, pp. 1001–1004.
- [34] L.W. Meyer, in: M.A. Meyers, L.E. Murr, K.P. Staudhammer (Eds.), *Shock-wave and High-strain-rate Phenomena in Materials*, Dekker, New York, 1992, pp. 49–68.
- [35] S.R. Chen, G.T. Gray III, *Comparison between the Mechanical Threshold Stress (Strength) Model and the New Zerilli–Armstrong Model*, Los Alamos National Laboratory, Report LA-UR-96-3594, October 1996.